

On-Chip Ge Photodetector Efficiency Enhancement by Local Laser-Induced Crystallization

Torgom Yezekyan,* Martin Thomaschewski, and Sergey I. Bozhevolnyi

Cite This: *Nano Lett.* 2021, 21, 7472–7478

Read Online

ACCESS |

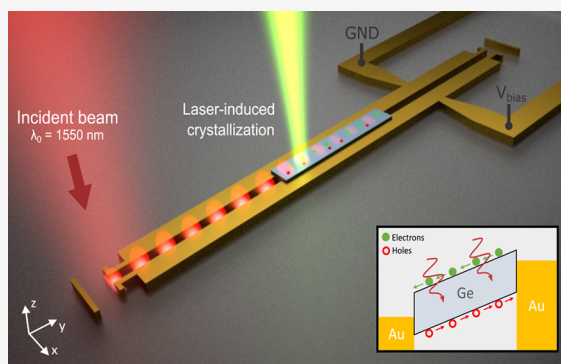
Metrics & More

Article Recommendations

Supporting Information

ABSTRACT: Metal–semiconductor–metal plasmonic nanostructures enable both on-chip efficient manipulation and ultrafast photodetection of strongly confined modes by enhancing local electrostatic and optical fields. The latter is achieved by making use of nanostructured thin-film germanium (Ge) plasmonic-waveguide photodetectors. While their sizes and locations can be accurately controlled during the nanofabrication, the detector efficiencies are significantly reduced due to deposited Ge amorphous nature. We demonstrate that the efficiency of waveguide-integrated Ge plasmonic photodetectors can be increased significantly (more than 2 orders of magnitude) by spatially controlled laser-induced Ge crystallization. We investigate both free-space and waveguide-integrated Ge photodetectors subjected to 800 nm laser treatment, monitoring the degree of crystallization with Raman spectroscopy, and demonstrate the efficiency enhancement by detecting the telecom radiation. The demonstrated local postprocessing technique can be utilized in various nanophotonic devices for efficient and ultrafast on-chip radiation monitoring and detection, offering significantly improved detector characteristics without jeopardizing the performance of other components.

KEYWORDS: surface plasmon polaritons, plasmonic waveguides, on-chip photodetection, laser-induced crystallization



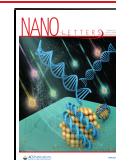
Photodetectors (PDs), i.e., optoelectronic devices converting light signals into electric currents, play a critical role in many optoelectronic applications, including optical communication and information processing, biochemical detection, and scientific research.^{1–6} An ever increasing demand for compact PD solutions can be met with monolithic integration of optical components and functionalities into ultracompact integrated photonic circuits.^{7–9} Consequently, addressing demands with respect to operation speeds, efficiencies, and critical feature sizes rivaling those found in electronics has triggered intense research in photonic components scaled down beyond the diffraction limit of light.^{10,11} In this context, surface plasmon polaritons (SPPs), electromagnetic excitations coupled to collective electron oscillations at metal–dielectric interfaces, constitute a promising concept, capable of concentrating and controlling optical signals using subwavelength structures.^{12,13}

Inevitably, whenever light interacts with metals, there occur optical (absorption) losses originating from resistive attenuation of electrical currents driven by electromagnetic fields.¹⁴ At the same time, there is hardly a way to avoid the use of metallic structures in optoelectronic devices that need electrical circuitry for their control. Bearing this in mind, one should properly design and utilize the metallic structures to make the best of their advantages, such as SPP localization and enhancement, while keeping optical absorption at bay. Employing metallic nanostructures in semiconductor materials as both signal electrodes and optical nanoantennas can

significantly improve the detector performance with respect to its compactness and thereby operation speed and efficiency.¹⁵ In metal–semiconductor–metal (MSM) plasmonic configurations, strongly confined SPP modes enhance the light–semiconductor interaction, and the generated free carriers can efficiently be extracted by the same metallic structure supporting the SPP modes.^{15–17}

Two major characteristics of a PD are the photoresponsivity and temporal response, i.e., the operation speed. In this context, the crystallinity of the semiconductor materials used becomes of crucial importance. The simplest way of fabricating on-chip integrated semiconductor PDs is based on thermal evaporation that, however, results in the deposited material being amorphous with a lower charge mobility than that in its crystalline counterparts.¹⁸ The latter also implies an increased recombination rate, with the carrier lifetime being reduced to picoseconds,¹⁹ which can be a major drawback of using amorphous materials for PDs: since recombined carriers do not contribute to the photocurrent, the quantum efficiency

Received: March 30, 2021
Revised: August 24, 2021
Published: September 1, 2021



becomes drastically reduced. The microelectronics and photovoltaic industries have historically used various techniques of thermal annealing to improve the crystallinity of deposited amorphous semiconductor material.²⁰ These methods require however very high annealing temperatures, typically >900 °C, a circumstance that limits their use with thermally sensitive nanostructures. In some cases, the thermal budget can be improved due to the metal-induced crystallization,^{21,22} which is based on the effect that certain metals in contact with amorphous materials induce transformation from the amorphous to crystalline phase at relatively low temperatures (although this might result in doping of semiconductor materials leading to their poor operation for radiation detection). Instead, local exposure by a focused pulsed laser beam is a very fast and much more gentle crystallization technique, suitable even for fragile nanostructured configurations^{23–25} and not causing the semiconductor doping.

In this work, we demonstrate that the efficiency of waveguide-integrated germanium (Ge) plasmonic PDs can be increased significantly by postprocessing with spatially controlled laser-induced Ge crystallization. We fabricate and investigate both free-space and waveguide-integrated Ge PDs subjected to 800 nm laser treatment, monitoring the degree of crystallization with Raman spectroscopy, and characterizing their efficiency by directly detecting the telecom radiation normally incident or coupled into plasmonic waveguides. Due to the improved Ge electrical properties (charge mobility and recombination rate), the internal quantum efficiency (IQE) is found to increase by 1 and 2 orders of magnitude for free-space and waveguide-integrated Ge detectors, respectively.

The design of the plasmonic waveguide PD is illustrated in Figure 1. The excited propagating mode is confined in the subwavelength waveguide slot, which has a height of 100 nm and a width of 300 nm. The entire device is covered with a 300 nm thick dielectric layer (PMMA, $n_{\text{PMMA}} = 1.48$) to reduce mode leakage into the underlying SiO₂ substrate. The

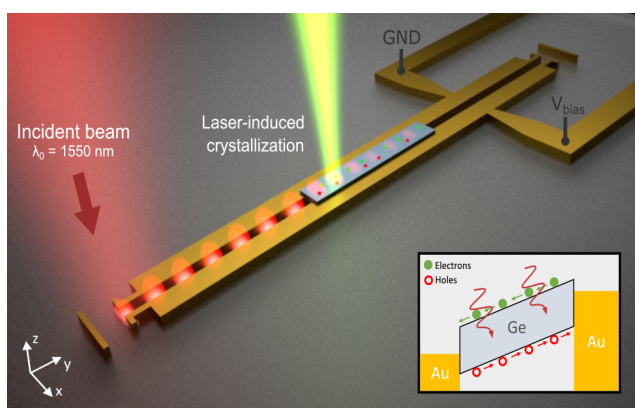


Figure 1. Three-dimensional rendering of the designed plasmonic waveguide PD. A 1550 nm laser beam is coupled to the plasmonic slot waveguide with the dipole antenna. The propagating waveguide mode is reaching the plasmonic MSM PD consisting of a Au–Ge–Au heterostructure, in which electron–hole pairs are generated upon mode absorption and subsequently collected by an externally applied reverse bias. A green beam is to indicate the laser treatment of a thin Ge stripe resulting in crystallization of deposited amorphous Ge. Inset: energy band diagram of the Au/Ge/Au heterojunction in the MSM PD under bias.

plasmonic detector is integrated into the waveguide structure by locally filling the slot with Ge semiconductor material.

The strongly confined SPP mode is absorbed by the Ge material, and the generated electron–hole pairs are collected by an external electric field. The inset in Figure 1 provides a schematic representation of the energy band diagram of the MSM heterostructure while the detector is biased with an externally applied voltage, which attracts the carriers toward the metal contact. The electrodes of the plasmonic PD are naturally integrated by the metal that supports the propagation of the corresponding SPP mode. Fabrication details of the proposed PD are given in the Fabrication section.

To understand the impact of laser-induced crystallization of Ge on its photovoltaic properties, we first discuss and analyze a free-space PD shown in Figure 2a. It consists of 100 nm thick gold electrodes of interdigital structure covered with 120 nm-thick Ge layer. The width of each electrode and the gap size between the electrodes are 1 μm, respectively. The incident radiation is absorbed in the Ge film, consequently leading to electron–hole pairs generation which are separated and accelerated by the electric field created by the externally applied bias voltage. These charge carriers are drifting toward the gold electrodes and generate a photocurrent which is proportional to the intensity of absorbed optical radiation.

To obtain optimal conditions for crystallization, we investigate the quality of crystallization while exposing a 120 nm-thick evaporated Ge film on a glass substrate with different values of laser average power. The laser source used for the crystallization was a mode-locked titanium–sapphire laser (Tsunami 3941 by Spectra-Physics), with a wavelength centered at 800 nm and pulse duration of less than 500 fs. Laser irradiation was focused with a high numerical aperture (NA = 0.9) objective to a diffraction-limited spot of ~450 nm. The sample was placed on a piezoelectric stage to allow scanning of the area that should be crystallized. The scanning speed was 20 μm/s with a laser spot overlap ratio of 85%.

Raman spectroscopy is a well-established technique for quantitative material characterization that can also be used to establish the crystallinity of materials.²⁶ Here, we used Raman spectroscopy to monitor the degree of crystallization of the Ge film, having a Ge monocrystalline wafer as a reference. It is worth mentioning that the amorphous state of a material is defined by randomly distributed small crystal grains, so that there is no sign of a macroscopic organized lattice pattern. In contrast, the crystalline state is defined as a fully organized lattice pattern of the material. Nevertheless, we will refer to the material as crystalline if the crystal grain distribution is organized enough within the area of laser illumination (meaning the laser used during Raman spectroscopy). Let us also mention that the spot size of the Raman microscope is nearly two times smaller than the illumination spot which was used for the crystallization. Figure 2b shows Raman spectra of a Ge thin film exposed to different laser powers (green, light, and dark blue curves) and Ge monocrystalline wafer (red curve) as well as a sample which was annealed by heat at 500 °C for 1 h (orange curve). Parameters for heat annealing at relatively low temperatures were chosen according to ref 27. It is clearly seen that the monocrystalline Ge wafer exhibits a stronger peak and narrow spectrum rather than evaporated Ge. Laser-induced crystallization at the laser power of 6 mW appears to be the most efficient among the investigated crystallization procedures. The Ge film annealed by macroscopic heating is showing a lower degree of crystallization

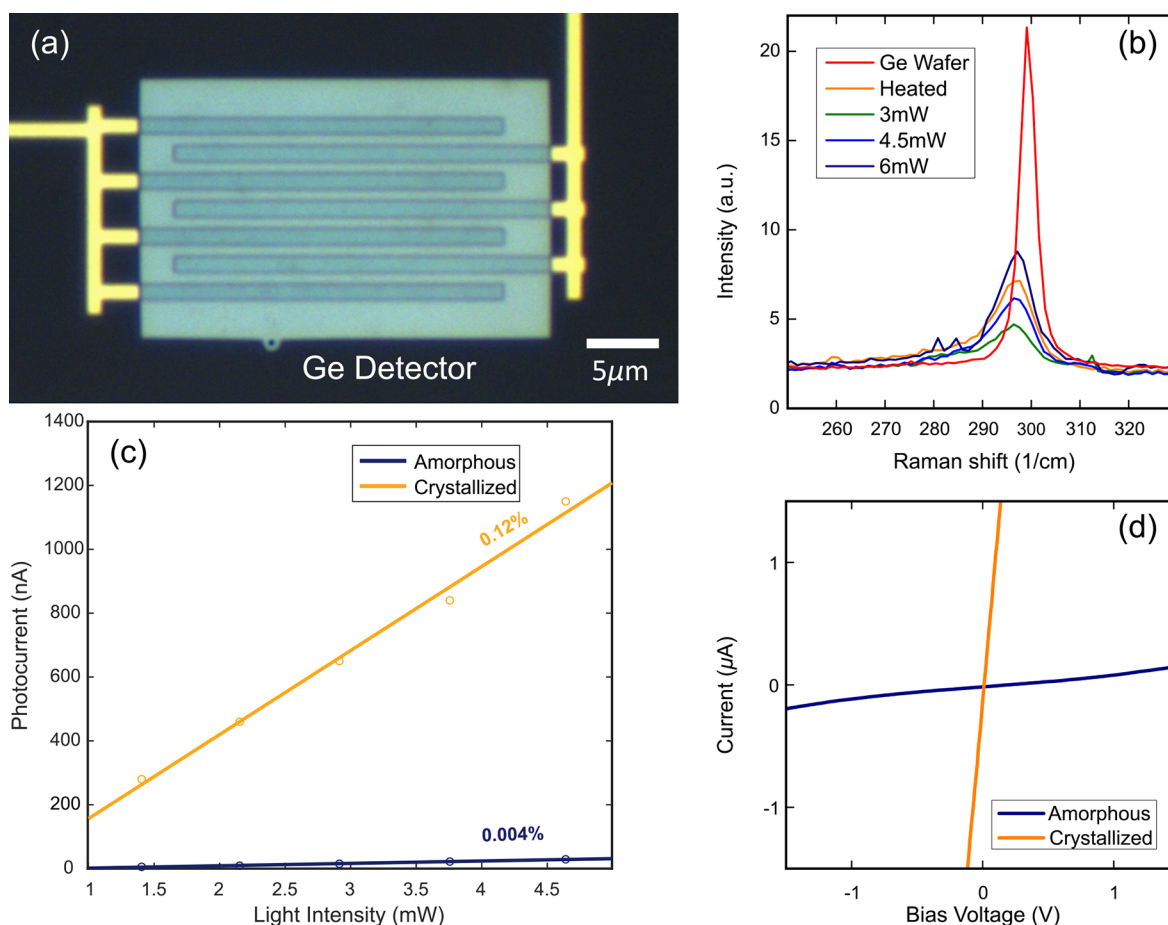


Figure 2. Characterization of the fabricated Ge PD with interdigital contacts before and after laser crystallization. (a) Optical image of the fabricated device. (b) Raman spectroscopy of the Ge thin film at different stages of laser-induced crystallization, indicating the laser power used (see text). A Ge monocrystalline wafer is used as a reference. (c) Photocurrent as a function of the incident 1550 nm light power before (blue line and circles) and after (orange line and circles) laser crystallization. The derived IQEs in percentage are indicated on their respective fitted lines. (d) Measured dark current–voltage curves before (blue curve) and after (orange curve) laser crystallization.

compared to the local laser-induced crystallization. This may originate from the pulse duration of the used laser (<500 fs), which in addition to the thermal impact may introduce certain nonthermal transitions in semiconductors.²⁸

One more peculiarity of the crystallization procedure is related to the differences between absorption and transmission spectra of amorphous and crystallized Ge. Any change of the material that leads to a larger size of Ge crystal grains reduces absorption and increases transmission of the light, particularly in the wavelength region where our laser is operating (800 nm).²⁹ This provides an additional opportunity to expose the same area of thin film to laser several times to achieve better and more homogeneous crystallization without the ablation of Ge material due to the absorption of laser radiation.

Photoelectrical properties of the Ge PD were measured before and after femtosecond pulsed laser treatment of the active layer of Ge. For the crystallization, the laser average power was set to 6 mW. Figure 2d plots the current–voltage measurements without any external illumination, i.e., dark current measurements before (blue curve) and after (orange curve) laser crystallization. One can note that the dark current of the crystallized Ge detector is much larger (by several orders of magnitude) than that of the amorphous counterpart, but nevertheless this is the price one should pay to increase the carrier mobility and lifetime and, hence, the efficiency of light

intensity–photocurrent conversion. It is worth mentioning that the current–voltage characteristics in both cases are nonlinear due to the Schottky type contact (see the full-scale plots in the Supporting Information S1).

Finally, Figure 2c provides the measured photocurrent as a function of the incident light intensity at $\lambda = 1550$ nm before (blue line and circles) and after (orange line and circles) laser crystallization. The bias voltage is set to 100 mV. In both cases, the photocurrent is linearly dependent on the light intensity. As a figure of merit, we also derived the IQE of the Ge PD which is added in percentage to the respective fitted lines. The enhancement of the IQE is evident. An improvement by more than 1 order of magnitude was achieved with this simple and quick material processing technique.

With this promising performance improvement in the free-space detector, we now discuss the Ge PD integrated in a plasmonic waveguide. As mentioned before, the system consists of a straight plasmonic waveguide equipped with coupling nanoantennas³⁰ locally filled with Ge. The scanning electron microscopy (SEM) image of the structure is shown in Figure 3a.

The propagating mode of the waveguide is excited when the incident beam is positioned at the coupling nanoantenna, with the polarization directed along the long axes of the nanoantenna arm. The launched plasmonic mode propagates

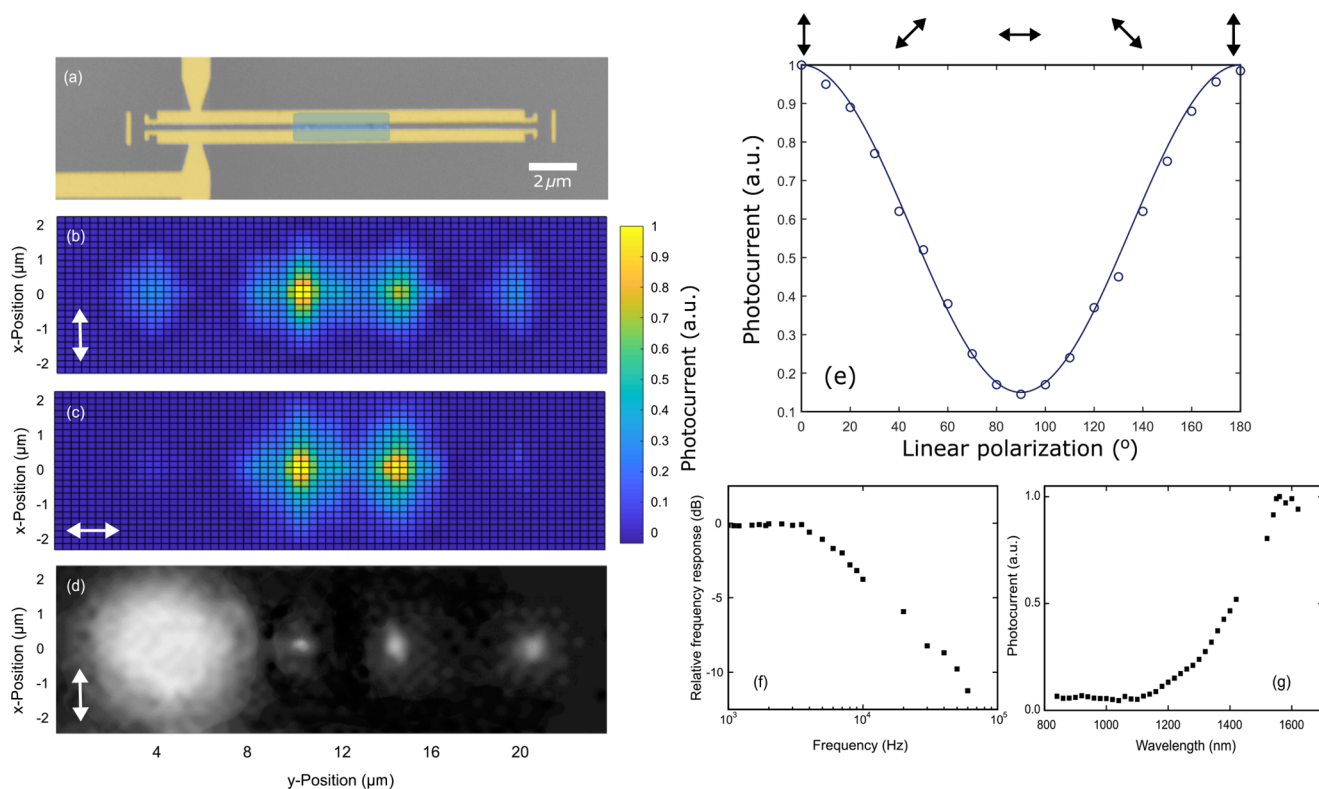


Figure 3. Characterization of the fabricated plasmonic waveguide Ge PD at 1550 nm wavelength. (a) Colorized scanning electron microscopy (SEM) image showing the top view of a plasmonic device. The Ge stripe (azure color) embedded in the plasmonic slot waveguide and forming the plasmonic Ge PD can readily be observed in the SEM image. (b, c) Two-dimensional photocurrent maps obtained by raster scanning the incident Gaussian beam polarized perpendicular and parallel to the waveguide axis, respectively. (d) Infrared camera image of the waveguide PD, when the left coupling antenna is illuminated, indicating mode scattering at the edges of the Ge stripe and outcoupling by the right antenna. (e) Photocurrent measured as a function of the polarization angle of the incident beam positioned at the left coupling antenna. (f) Frequency response measurements of the plasmonic waveguide Ge PD indicate a -3 dB bandwidth of ~ 10 kHz, being limited by the response time of the signal amplifier used. (g) Wavelength dependence of the photocurrent.

toward the Ge detector, penetrating a $5 \mu\text{m}$ long MSM region, while the full length of the plasmonic waveguide is $15 \mu\text{m}$. With the same mechanism that was described before, the SPPs are absorbed in the Ge material, consequently producing photoinduced current. The realization of the on-chip detection is becoming evident from the spatial photocurrent maps obtained by raster scanning the incident Gaussian beam (Figure 3b,c) as well as from the clear polarization dependency when excited at the coupling nanoantenna (Figure 3e). In all measurements, the wavelength of the incident beam is 1550 nm, and the calculated coupling efficiency to the plasmonic waveguide is 6%, while the mode propagation length is $8.5 \mu\text{m}$. As a matter of a fact, the propagation losses in the plasmonic waveguide strongly attenuate the light intensity that reaches the waveguide detector (i.e., the MSM region). For this reason, the measured photocurrent is much larger when the incident beam is focused at the edges of Ge strip rather than when it is positioned at the coupling nanoantennas (Figure 3b,c). We also measured the frequency response of the plasmonic waveguide Ge PD as well as the wavelength dependence of the photocurrent (Figure 3f,g). The first shows a -3 dB bandwidth of ~ 10 kHz, which is entirely limited by the response time of the signal amplifier used for measurements. The proposed structure will be capable for high-speed detection due to low electrical capacity (~ 10 fF) and high carrier mobility along with low recombination rate originated from the laser-induced crystallization. It is worth mentioning

that measuring the wavelength dependence of the photocurrent (Figure 3g), we positioned the Gaussian beam directly on the Ge stripe rather than the coupling nanoantenna to minimize the wavelength limitations associated with the plasmonic waveguide.

Like the case with Ge PD discussed in the beginning, here we will also use the same characteristics to investigate the plasmonic waveguide Ge PD performance before and after laser-induced crystallization. The crystallization procedure was the same as in the case of the free-space PD. We performed numerical simulations to estimate the average laser power at which the Ge material will be melted (Supporting Information, S2). Please note that not only the laser intensity but also the scanning speed (controlled with the motorized stage) and germanium deposition procedure (every time the degree of crystallization in the gap is slightly different) affect the crystallization process. Hence, the threshold of the laser intensity and the most suitable scanning speed were established empirically. For the plasmonic waveguide PD the effect of crystallization was already pronounced at an average laser power of 4 mW as verified with the Raman spectrum recording and dark current–voltage characterization. However, the most efficient crystallization was achieved when the laser power was 8 mW at the scanning speed of $20 \mu\text{m/s}$. It should be noted that the Au stripes of the plasmonic waveguide are working as heat sinks for Ge during the laser treatment and the degree of crystallization is relatively small in the case of small

gaps (<200 nm). For this reason, we chose a gap size of 300 nm where the effect of crystallization is strongly pronounced. Figure 4a shows the Raman spectra of the Ge stripe before

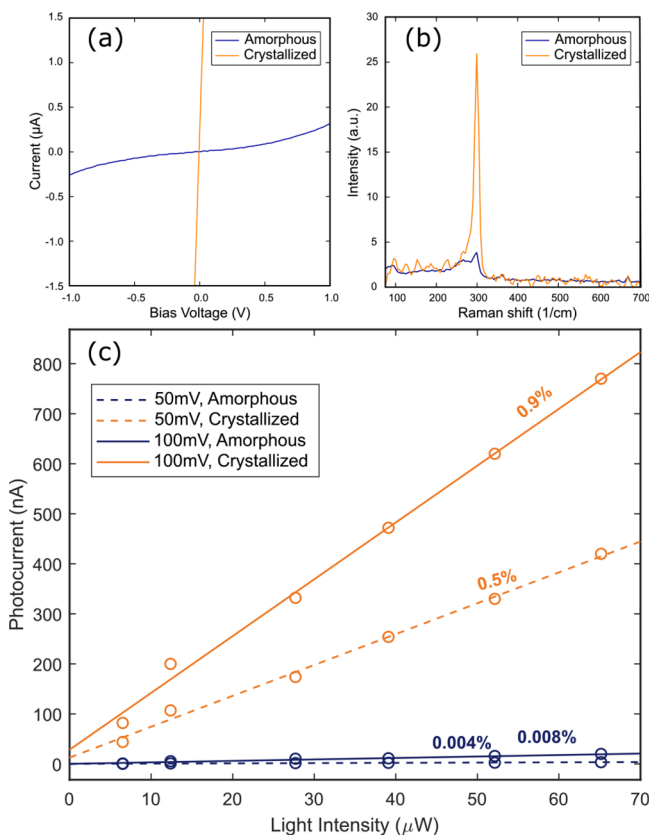


Figure 4. Characteristics of the plasmonic waveguide Ge PD before and after laser-induced crystallization with the laser power of 8 mW. (a) Measured dark current–voltage curves before (blue curve) and after (orange curve) laser crystallization. (b) Raman spectroscopy of the Ge stripe before (blue curve) and after (orange curve) laser-induced crystallization. (c) Photocurrent as a function of the incident 1550 nm light power before (blue lines and circles) and after (orange lines and circles) laser-induced crystallization for various applied bias voltages. The derived IQEs in percentage are indicated on their respective fitted lines.

(blue curve) and after (orange curve) laser-induced crystallization. The fs laser intensity was set to 8 mW. Next the dark current was measured, which again is showing a great enhancement after the crystallization (Figure 4b). Finally, we measured the photocurrent of the plasmonic waveguide Ge PD for different values of absorbed power at two different bias voltages (Figure 4c), before (blue lines and circles) and after crystallization (orange lines and circles). Here it is worth mentioning that the calculated IQEs are underestimated, as we assumed that the whole energy reaching the Ge strip is fully absorbed, while it appeared to be not entirely correct, as shown in Figure 3d. An infrared camera image of the waveguide PD, when the left coupling antenna is illuminated, reveals that the mode is scattered at the edges of the Ge strip as well as at the opposite (outcoupling) nanoantenna. Another limitation was caused by the amplifier used to enhance the photocurrent, which became saturated at relatively low bias voltages (200 mV), so we had to use lower bias voltages, limiting thereby the achievable IQE levels. Nevertheless, as we focus in this study on the relative enhancement of the IQE due to laser-induced

crystallization, we will disregard the resulting underestimation of the IQE. For the bias voltages of 50 mV and 100 mV, the IQEs before crystallization are 0.004% and 0.008%, respectively, whereas after the laser treatment one obtains 0.5% and 0.9%, respectively, revealing the drastic improvement of the IQE by 2 orders of magnitude.

In summary, we fabricated and investigated free-space and waveguide-integrated Ge PDs and demonstrate the efficiency enhancement by detecting the telecom radiation. We show that the degree of crystallization can be increased by local ultrafast pulsed laser processing without any damage to the device. In situ characterization of the modification of crystallization in the semiconductor was conducted by Raman spectroscopy. Due to the laser-induced crystallization, the measured IQE of the free-space Ge PD was significantly increased by more than 1 order of magnitude, while for the plasmonic waveguide Ge PD the IQE was enhanced by 2 orders of magnitude.

The time response of the proposed PD is mainly determined by the PD capacitance, carrier mobility, and carrier recombination rate in Ge. Due to a very small size, the capacitance of our device is as small as ~10 fF. Furthermore, the laser-induced crystallization of semiconductors (transition from amorphous to polycrystalline) is leading to the increase of the carrier mobility.³¹ Additionally, due to a small gap, the accelerating field acting on electrons is very high, forcing electrons to drift at velocities comparable with those found in monocrystalline structures.³² Finally, the recombination rate is faster in (partially) polycrystalline Ge in comparison with that in a monocrystalline one. Bearing all these factors in mind, one should expect finding a very fast response (>100 GHz¹⁶) in the proposed PD.

The presented devices can be integrated in various nanophotonic and nanoplasmonic structures for on-chip detection, with significantly improved optoelectronic characteristics and local modification capabilities by laser-induced semiconductor crystallization.

Fabrication. The fabrication of the device relies on a multistep lithographic process using the mix-and-match technique for lithographic overlay. First, bonding pads and connecting electrodes are patterned onto a glass chip by optical lithography, metal deposition (5 nm Ti/50 nm Au) and liftoff. The plasmonic circuits are written by electron-beam lithography (EBL) at an acceleration voltage of 30 keV in a 300 nm PMMA resist and 20 nm thick Al layer to prevent charge accumulation. The alignment between the different lithography steps is performed manually using markers. After development, the waveguides are formulated by depositing a 5 nm titanium adhesion layer and 100 nm gold by thermal evaporation and subsequent 12 h lift-off in acetone. For the optical characterization, a 300 nm PMMA cladding was spin-coated on the chip to reduce mode leakage into the glass substrate. The same PMMA layer serves as an electron beam resist for the last EBL step, which integrates the germanium PDs onto the plasmonic circuit by evaporating 2 nm Ti and 120 nm Ge onto the predefined region. The germanium material is evaporated in a sufficiently outgassed tungsten boat to prevent impurities during deposition. Finally, a 300 nm thin layer of PMMA is deposited.

IQE Calculation. IQE was calculated according to

$$\text{IQE} = 100 \left(\frac{I_{ph}}{P_{abs} \cdot \lambda} \right) \left(\frac{hc}{e} \right)$$

where I_{ph} is the measured photocurrent, P_{abs} is the absorbed power by the PD, λ is the wavelength, e is the elementary charge, and h and c are the Planck constant and speed of light, respectively.

■ ASSOCIATED CONTENT

Supporting Information

The Supporting Information is available free of charge at <https://pubs.acs.org/doi/10.1021/acs.nanolett.1c01281>.

Full scale dark current–voltage characteristics of the photodetector, numerical simulations, and study of the power dependence of the germanium temperature (PDF)

■ AUTHOR INFORMATION

Corresponding Author

Torgom Yezekyan – Centre for Nano Optics, University of Southern Denmark, DK-5230 Odense M, Denmark;
orcid.org/0000-0003-2019-2225; Email: ty@mci.sdu.dk

Authors

Martin Thomaschewski – Centre for Nano Optics, University of Southern Denmark, DK-5230 Odense M, Denmark;
orcid.org/0000-0003-2545-1468

Sergey I. Bozhevolnyi – Centre for Nano Optics, University of Southern Denmark, DK-5230 Odense M, Denmark;
orcid.org/0000-0002-0393-4859

Complete contact information is available at:
<https://pubs.acs.org/doi/10.1021/acs.nanolett.1c01281>

Funding

The authors acknowledge the financial support from Villum Fonden, Award in Technical and Natural Sciences 2019. T.Y. acknowledges funding from MULTIPLY fellowship under the Marie Skłodowska-Curie COFUND Action (Grant Agreement No. 713694).

Notes

The authors declare no competing financial interest.

■ ACKNOWLEDGMENTS

We acknowledge Saskia Fiedler for her help in capturing the SEM images.

■ REFERENCES

- (1) Garcia de Arquer, F. P.; Armin, A.; Meredith, P.; Sargent, E. H. Solution-processed semiconductors for next-generation photodetectors. *Nature Reviews Materials* **2017**, *2*, 16100.
- (2) Koppens, F.; Mueller, T.; Avouris, P.; Ferrari, A.; Vitiello, M.; Polini, M. Photodetectors based on graphene, other two-dimensional materials and hybrid systems. *Nat. Nanotechnol.* **2014**, *9*, 780–793.
- (3) Long, M.; Wang, Y.; Wang, P.; Zhou, X.; Xia, H.; Luo, C.; Huang, S.; Zhang, G.; Yan, H.; Fan, Z.; et al. Palladium diselenide long-wavelength infrared photodetector with high sensitivity and stability. *ACS Nano* **2019**, *13*, 2511–2519.
- (4) Maria, A.; Cyr, P. W.; Klem, E. J.; Levina, L.; Sargent, E. H. Solution-processed infrared photovoltaic devices with > 10% monochromatic internal quantum efficiency. *Appl. Phys. Lett.* **2005**, *87*, 213112.
- (5) Simone, G.; Dyson, M. J.; Meskers, S. C.; Janssen, R. A.; Gelinck, G. H. Organic photodetectors and their application in large area and flexible image sensors: the role of dark current. *Adv. Funct. Mater.* **2020**, *30*, 1904205.

(6) Zhou, X.; Yang, D.; Ma, D. Extremely Low Dark Current, High Responsivity, All-Polymer Photodetectors with Spectral Response from 300 to 1000 nm. *Adv. Opt. Mater.* **2015**, *3*, 1570–1576.

(7) Gerrits, T.; Thomas-Peter, N.; Gates, J. C.; Lita, A. E.; Metcalf, B. J.; Calkins, B.; Tomlin, N. A.; Fox, A. E.; Linares, A. L.; Spring, J. B.; et al. On-chip, photon-number-resolving, telecommunication-band detectors for scalable photonic information processing. *Phys. Rev. A: At., Mol., Opt. Phys.* **2011**, *84*, 060301.

(8) Schwarz, B.; Reininger, P.; Ristanić, D.; Detz, H.; Andrews, A. M.; Schrenk, W.; Strasser, G. Monolithically integrated mid-infrared lab-on-a-chip using plasmonics and quantum cascade structures. *Nat. Commun.* **2014**, *5*, 4085.

(9) Najafi, F.; Mower, J.; Harris, N. C.; Bellei, F.; Dane, A.; Lee, C.; Hu, X.; Kharel, P.; Marsili, F.; Assefa, S.; et al. On-chip detection of non-classical light by scalable integration of single-photon detectors. *Nat. Commun.* **2015**, *6*, 5873.

(10) Ebbesen, T. W.; Genet, C.; Bozhevolnyi, S. I. Surface-plasmon circuitry. *Phys. Today* **2008**, *61*, 44.

(11) Sorger, V. J.; Oulton, R. F.; Ma, R.-M.; Zhang, X. Toward integrated plasmonic circuits. *MRS Bull.* **2012**, *37*, 728–738.

(12) Gramotnev, D. K.; Bozhevolnyi, S. I. Plasmonics beyond the diffraction limit. *Nat. Photonics* **2010**, *4*, 83–91.

(13) Ozbay, E. Plasmonics: merging photonics and electronics at nanoscale dimensions. *Science* **2006**, *311*, 189–193.

(14) Baffou, G.; Quidant, R. Thermo-plasmonics: using metallic nanostructures as nano-sources of heat. *Laser & Photonics Reviews* **2013**, *7*, 171–187.

(15) Fan, P.; Huang, K. C.; Cao, L.; Brongersma, M. L. Redesigning photodetector electrodes as an optical antenna. *Nano Lett.* **2013**, *13*, 392–396.

(16) Salamin, Y.; Ma, P.; Baeuerle, B.; Emboras, A.; Fedoryshyn, Y.; Heni, W.; Cheng, B.; Josten, A.; Leuthold, J. 100 GHz plasmonic photodetector. *ACS Photonics* **2018**, *5*, 3291–3297.

(17) Thomaschewski, M.; Yang, Y.; Wolff, C.; Roberts, A. S.; Bozhevolnyi, S. I. On-chip detection of optical spin–orbit interactions in plasmonic nanocircuits. *Nano Lett.* **2019**, *19*, 1166–1171.

(18) Sorianello, V.; Colace, L.; Armani, N.; Rossi, F.; Ferrari, C.; Lazzarini, L.; Assanto, G. Low-temperature germanium thin films on silicon. *Opt. Mater. Express* **2011**, *1*, 856–865.

(19) Auston, D.; Lavallard, P.; Sol, N.; Kaplan, D. An amorphous silicon photodetector for picosecond pulses. *Appl. Phys. Lett.* **1980**, *36*, 66–68.

(20) Hosoi, T.; Suzuki, Y.; Shimura, T.; Watanabe, H. Mobility characterization of Ge-on-insulator metal-oxide-semiconductor field-effect transistors with striped Ge channels fabricated by lateral liquid-phase epitaxy. *Appl. Phys. Lett.* **2014**, *105*, 173502.

(21) Herd, S.; Chaudhari, P.; Brodsky, M. H. Metal contact induced crystallization in films of amorphous silicon and germanium. *J. Non-Cryst. Solids* **1972**, *7*, 309–327.

(22) Wang, Z.; Wang, J.; Jeurgens, L.; Mittemeijer, E. Thermodynamics and mechanism of metal-induced crystallization in immiscible alloy systems: Experiments and calculations on Al/a-Ge and Al/a-Si bilayers. *Phys. Rev. B: Condens. Matter Mater. Phys.* **2008**, *77*, 045424.

(23) Choi, T. Y.; Hwang, D. J.; Grigoropoulos, C. P. Ultrafast laser-induced crystallization of amorphous silicon films. *Opt. Eng.* **2003**, *42*, 3383–3388.

(24) Shieh, J.-M.; Chen, Z.-H.; Dai, B.-T.; Wang, Y.-C.; Zaitsev, A.; Pan, C.-L. Near-infrared femtosecond laser-induced crystallization of amorphous silicon. *Appl. Phys. Lett.* **2004**, *85*, 1232–1234.

(25) Cao, J.; Lancry, M.; Brisset, F.; Mazerolles, L.; Saint-Martin, R.; Poumellec, B. Femtosecond laser-induced crystallization in glasses: growth dynamics for orientable nanostructure and nanocrystallization. *Cryst. Growth Des.* **2019**, *19*, 2189–2205.

(26) Smit, C.; Van Swaaij, R.; Donker, H.; Petit, A.; Kessels, W.; Van de Sanden, M. Determining the material structure of microcrystalline silicon from Raman spectra. *J. Appl. Phys.* **2003**, *94*, 3582–3588.

(27) Blum, N. A.; Feldman, C. The crystallization of amorphous germanium films. *J. Non-Cryst. Solids* **1976**, *22*, 29–35.

(28) Sundaram, S.; Mazur, E. Inducing and probing non-thermal transitions in semiconductors using femtosecond laser pulses. *Nat. Mater.* **2002**, *1*, 217–224.

(29) Bermejo, D.; Cardona, M. Infrared absorption in hydrogenated amorphous and crystallized germanium. *J. Non-Cryst. Solids* **1979**, *32*, 421–430.

(30) Kriesch, A.; Burgos, S. P.; Ploss, D.; Pfeifer, H.; Atwater, H. A.; Peschel, U. Functional plasmonic nanocircuits with low insertion and propagation losses. *Nano Lett.* **2013**, *13*, 4539–4545.

(31) Watakabe, H.; Sameshima, T.; Kanno, H.; Miyao, M. Electrical properties for poly-Ge films fabricated by pulsed laser annealing. *Thin Solid Films* **2006**, *508*, 315–317.

(32) Gu, Q.; Schiff, E.; Chévrier, J.-B.; Equer, B. High-field electron-drift measurements and the mobility edge in hydrogenated amorphous silicon. *Phys. Rev. B: Condens. Matter Mater. Phys.* **1995**, *52*, 5695.

Supporting Information for

On-chip Ge photodetector efficiency enhancement by local laser-induced crystallization

Torgom Yezekyan, Martin Thomaschewski, Sergey I. Bozhevolnyi*

AUTHOR ADDRESS. Centre for Nano Optics, University of Southern Denmark, Campusvej 55,
DK-5230 Odense M, Denmark

*Corresponding author: ty@mci.sdu.dk

S1: Full scale dark current-voltage characteristics

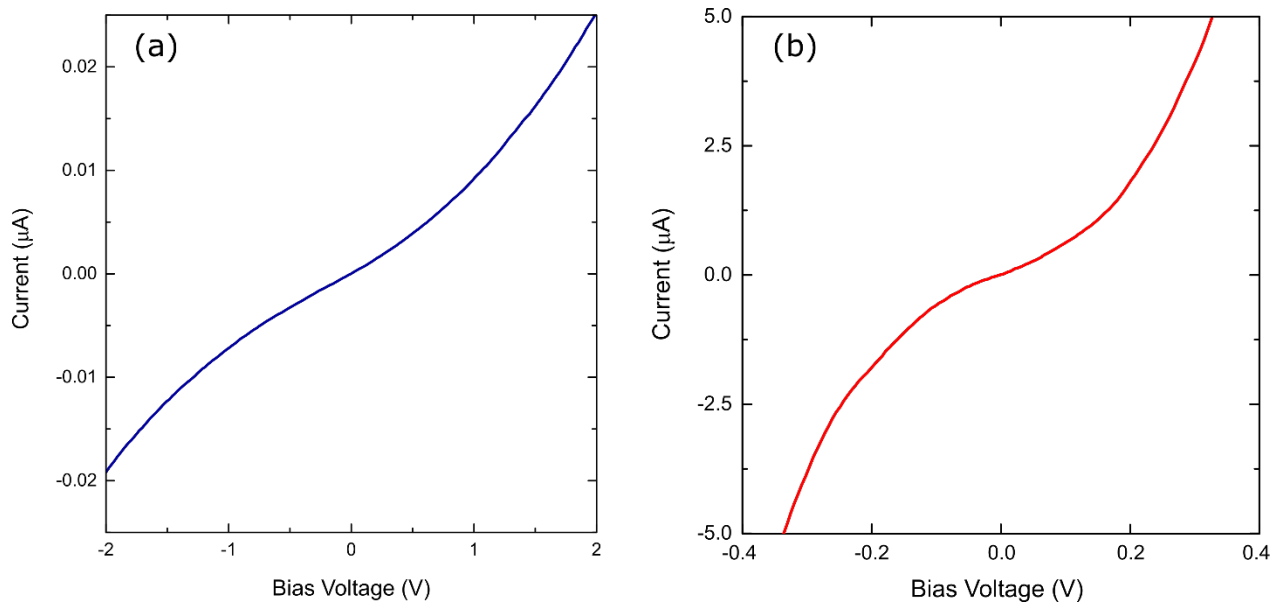


Figure S1 Full scale dark current–voltage characteristics of free space Ge PD before (a) and after (b) laser crystallization.

S2: Numerical study of power dependence of the Ge temperature

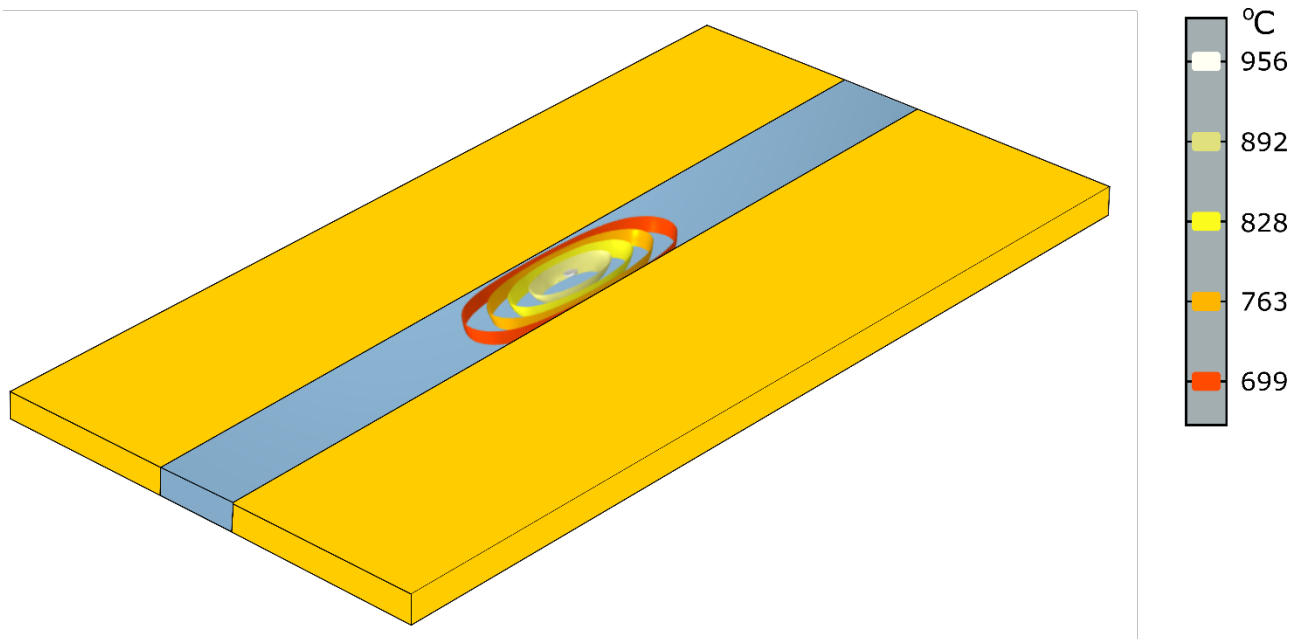


Figure S2. Isothermal contours in the Ge stripe sandwiched between gold claddings at laser average power of 3mW and exposure time of 30ms. The focused laser beam was simulated as a Gaussian beam with corresponding waist. In this case Ge temperature in the center of the laser beam exceeds its melting point (938.2 °C) while the temperature near the metal stripes (red contour), as expected, is largely smaller than in the central part (27 %).

Simulations were carried out in Comsol Multiphysics 5.6, we used a combination of Wave optics and Heat transfer modules. As a source of radiation, we used a Gaussian beam with a beam waist corresponding to the laser beam spot size in the real experiment. We assumed a perfect contact between germanium and gold stripes and considered the absorption coefficient of the germanium not being dependent on the temperature.

Table S2: Estimated temperatures in the center of Gaussian beam for different laser powers according to the simulations.

Avg Power (mW)	Temp. (°C)
3	963
3.5	1065
4	1167
5	1367